Binding of anisotropic curvature–inducing proteins onto membrane tubes

Journal:	*Soft Matter*
Manuscript ID	SM-ART-02-2022-000274.R1
Article Type:	Paper
Date Submitted by the Author:	30-Mar-2022
Complete List of Authors:	Noguchi, Hiroshi; University of Tokyo, Institute for Solid State Physics Tozzi, Caterina; Universitat Politècnica de Catalunya, ORCID iD: 0000-0002-9105-798X; Vall d'Hebron Institute of Oncology Arroyo, Marino; Universitat Politècnica de Catalunya,

Journal Name

Binding of anisotropic curvature-inducing proteins onto membrane tubes[†]

Hiroshi Noguchi,[*,a] Caterina Tozzi,[be] and Marino Arroyo[bcd]

Bin/Amphiphysin/Rvs superfamily proteins and other curvature-inducing proteins have anisotropic shapes and anisotropically bend biomembrane. Here, we report how the anisotropic proteins bind the membrane tube and are orientationally ordered using mean-field theory including an orientation-dependent excluded volume. The proteins exhibit a second-order or first-order nematic transition with increasing protein density depending on the radius of the membrane tube. The tube curvatures for the maximum protein binding and orientational order are different and varied by the protein density and rigidity. As the external force along the tube axis increases, a first-order transition from a large tube radius with low protein density to a small radius with high density occurs once, and subsequently, the protein orientation tilts to the tube-axis direction. When an isotropic bending energy is used for the proteins with an elliptic shape, the force-dependence curves become symmetric and the first-order transition occurs twice. This theory quantitatively reproduces the results of meshless membrane simulation for short proteins, whereas deviations are seen for long proteins owing to the formation of protein clusters.

1 Introduction

In living cells, numerous types of proteins work together to regulate biomembrane shapes of cells and organelles[1–8]. Proteins are also involved in dynamic processes such as endo-/exocytosis, vesicle transport, cell locomotion, and cell division. Clathrin and coat protein complex (COPI and COPII) bend membranes in a laterally isotropic manner and generate spherical buds[3–6]. On the contrary, Bin/Amphiphysin/Rvs (BAR) superfamily proteins bend the membrane anisotropically and generate cylindrical membrane tubes[1–3,9–16]. The BAR domains consist of a banana-shaped dimer and bend the membrane along its axis. Dysfunctions of the BAR proteins are considered to be implicated in neurodegenerative, cardiovascular, and neoplastic diseases. Thus, understanding the mechanism of the curvature generation by these proteins is important.

The curvature-inducing proteins can sense the membrane curvature, i.e., they are concentrated in membranes that have their preferred curvatures. The sensing of curvature-inducing proteins,

such as BAR proteins[7,8,13,17,18], dynamin[19], and G-protein coupled receptors[20], has been examined using a tethered vesicle pulled by optical tweezers and a micropipette. They typically bind more onto the membrane tube than the remaining spherical component.

Theoretically, the bending energy of a single-component fluid membrane is well described by the second-order expansion to the curvature (Canham–Helfrich energy)[21,22]. The binding of proteins with a laterally isotropic spontaneous curvature is considered to locally change the coefficients of the Canham–Helfrich energy (the bending rigidity and spontaneous curvature). Budding[23–28] and other shape deformations[29,30] induced by protein binding have been well explained by mean-field theories using this bending energy. Moreover, traveling waves of membrane deformation can be reproduced by the coupling with reaction-diffusion of multiple types of proteins[31–34]. In contrast, the effects of the anisotropic spontaneous curvature of proteins have been much less explored. Instead, the bending energy for isotropic spontaneous curvature has been often used for the analysis of BAR proteins[17,18,32]. A few approaches have been examined for the anisotropy of the protein binding. The Canham–Helfrich energy was extended for anisotropic spontaneous curvature[35,36] and membrane-mediated interactions between non-deformable anisotropic objects have been investigated[37–40]. For cylindrical membranes, the axis of banana-shaped proteins were assumed aligned in the azimuthal direction to derive a force–extension curve[41]. However, the entropic interaction of the pro-

a Institute for Solid State Physics, University of Tokyo, Kashiwa, Chiba 277-8581, Japan. E-mail: noguchi@issp.u-tokyo.ac.jp
b Universitat Politècdnica de Catalunya-BarcelonaTech, 08034 Barcelona, Spain
c Institute for Bioengineering of Catalonia (IBEC), The Barcelona Institute for Science and Technology (BIST), 08028 Barcelona, Spain
d Centre Internacional de Mètodes Numèrics en Enginyeria (CIMNE), 08034 Barcelona, Spain
e Present address: Vall d'Hebron Institute of Oncology (VHIO), 08035 Barcelona, Spain
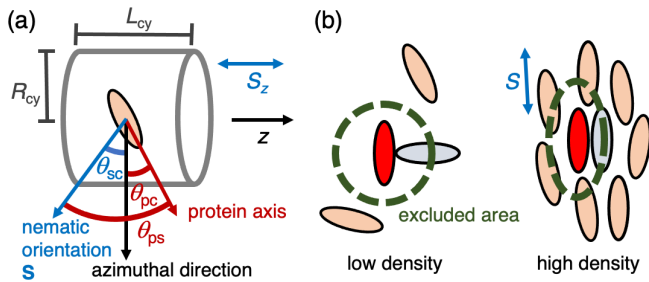
Fig. 1 Schematic of the theoretical model. (a) An elliptic protein on a membrane tube. The angles between the nematic direction $\mathbf{S}$, the azimuthal direction, and/or and protein axis. (b) Excluded-volume interactions between proteins. A perpendicular protein pair has a larger excluded area (represented by thick dashed lines) than a parallel pair, leading to a nematic order at a high density.

tein orientation has not been considered in these studies.

Recently, this entropic interaction was taken into account by two of us and co-workers[42,43] based on Nascimentos' theory for three-dimensional liquid-crystals[44]. An isotropic-to-nematic transition was obtained on a fixed membrane shape. In this study, we examine the binding of the anisotropic proteins to a cylindrical membrane tube in detail. The axial force along the membrane tube and equilibrium of protein binding/unbinding are considered. Moreover, we clearly show the difference from the binding of isotropic proteins[30]. The tube part of a tethered vesicle is well approximated by this tube with no volume constraint, when tube radius is much smaller than the vesicle radius[30].

Several types of membrane models have been developed for coarse-grained simulations[45–47]. The protein binding has been investigated using molecular simulations[48–54], dynamically triangulated membrane simulations[55,56], and meshless membrane simulations[40,41,57–61]. Among them, however, the binding effects on the axial force of a membrane tube have been investigated only by the meshless simulations[41,57,59]; a characteristic force dependence on the protein curvature was reported for homogeneous states at low protein curvatures, in addition to the protein assembly accompanied by membrane shape transformation at high protein curvatures. Here, we compare our theoretical results with those of the meshless simulations.

The mean-field theory is described in Sec. 2. Simulations of membrane tubes are described in Sec. 3. The simulation results are compared with the theoretical results in Sec. 3.2. Finally, a summary and discussion are presented in Sec. 4.

2   Theoretical analysis

2.1   Theory

Protein binding on a cylindrical membrane tube is considered as depicted in Fig. 1(a). The membrane is in a fluid phase and the surface area A is fixed. The radius and length of the tube are R_{cy} and L_{cy}: $A = 2\pi R_{cy}L_{cy}$. The tube volume can be freely changed. This corresponds to the tubular region of a tethered vesicle in the limit condition, in which the tube volume is negligibly small ($\pi R_{cy}^2 L_{cy} \ll V$, where V is the vesicle volume)[30,62]. Proteins can align in the membrane surface. To quantify it, the degree of the

orientational order is calculated as

$$S = 2\langle s_p(\theta_{ps})\rangle, \tag{1}$$

$$s_p(\theta_{ps}) = \cos^2(\theta_{ps}) - \frac{1}{2}, \tag{2}$$

where $\langle ... \rangle$ is the ensemble average, and θ_{ps} is the angle between the major protein axis and the ordered direction. The angles between the ordered direction and the azimuthal direction of the cylinder and between the major protein axis and azimuthal direction are θ_{sc} and θ_{pc}, respectively, with $\theta_{ps} = \theta_{pc} + \theta_{sc}$ (see Fig. 1(a)). Experimentally, the oritational order S_z along the tube (z) axis is more easily measured: for $\theta_{sc} = 0$ and $\pi/2$, $S_z = -S$ and $S_z = S$, respectively.

The bound protein is approximated to have laterally an elliptic shape with an aspect ratio of $d_{el} = \ell_1/\ell_2$ and area $a_p = \pi\ell_1\ell_2/4$, where ℓ_1 are ℓ_2 are the lengths in the major and minor axes, respectively. An orientation-dependent excluded-volume interaction is considered between proteins. When two proteins are perpendicularly oriented, the excluded area A_{exc} between them is larger than the parallel pairs, as shown in Fig. 1(b). This area A_{exc} is expressed as $A_{exc} = B_0 + B_2(\cos^2(\theta_{pp}) - 1/2) + O(\cos^4(\theta_{pp}))$ by a Taylor expansion, where θ_{pp} is the angle between the major axes of two ellipses. In our previous study[42], the values of B_0 and B_2 are calculated by a two-parameter fit. In this study, the one-parameter fit of $A_{exc} = [4 - b_{exc}(\cos^2(\theta_{pp}) - 1)]a_p$ is used, since the minimum value $A_{exc}^{min} = 4a_p$ is obtained at the parallel pairs ($\theta_{pp} = 0$) for any ratio of d_{el}: $b_{exc} = 0.840$, 1.98, 3.44, and 7.61 at $d_{el} = 2$, 3, 4, and 7, respectively. The effective excluded area is represented by $A_{eff} = \lambda A_{exc}$. The parameter λ is a function of the protein density and $\lambda = 1/2$ at a low-density limit[44]. At the close-packed condition, the area fraction ϕ of the bound protein has the maximum: $\phi_{max} = a_p/\lambda A_{exc}^{min} = 1/4\lambda = \pi/2\sqrt{3} \approx 0.907$ in two-dimensional space[63]. For simplicity, we use a constant value, $\lambda = 1/3$, as in our previous study[42,43], i.e., $\phi_{max} = 0.75$. In this study, we consider no attractive interactions between the proteins and focus on isotropic and nematic phases, such that smectic and crystal phases are not in the scope.

The bending energy of the bare (unbound) membrane is given by

$$U_{mb} = \int \frac{\kappa_d}{2}(C_1 + C_2)^2 dA = \frac{\kappa_d A}{2R_{cy}^2}, \tag{3}$$

where C_1 and C_2 are the principal curvatures ($C_1 = 1/R_{cy}$ and $C_2 = 0$ for the cylinder). The unbound membrane has a bending rigidity κ_d and zero spontaneous curvature. The tubular membrane is connected to a large lipid reservoir, and the area difference elasticity[64,65] is negligible. The bound protein gives an additional bending energy as $\langle U \rangle = U_{mb} + N_p\langle U_p\rangle$, where $N_p = \phi A/a_p$ is the number of the bound protein and U_p is the bending energy of one protein. The protein has an anisotropic bending energy:

$$U_p = \frac{\kappa_p a_p}{2}(C_{\ell 1} - C_p)^2 + \frac{\kappa_{side} a_p}{2}(C_{\ell 2} - C_{side})^2, \tag{4}$$

$$C_{\ell 1} = C_1\cos^2(\theta_{pc}) + C_2\sin^2(\theta_{pc}), \tag{5}$$

$$C_{\ell 2} = C_1\sin^2(\theta_{pc}) + C_2\cos^2(\theta_{pc}), \tag{6}$$

where $C_{\ell 1}$ and $C_{\ell 2}$ are curvatures along the major and minor axes of the proteins, respectively. κ_p and C_p are the bending rigidity and spontaneous curvature along the major protein axis, respectively, and κ_{side} and C_{side} are those along the minor axis (side direction). Here, $\kappa_{side} = 0$ is used unless otherwise specified.

The free energy F_p of the bound proteins is expressed as

$$F_p = \int f_p \, dA, \qquad (7)$$

$$f_p = \frac{\phi k_B T}{a_p}\left[\ln(\phi) + \frac{S\Psi}{2} - \ln\left(\int_{-\pi/2}^{\pi/2} w(\theta_{ps}) \, d\theta_{ps}\right)\right], \quad (8)$$

$$w(\theta_{ps}) = g\exp[\Psi s_p(\theta_{ps}) + \bar{\Psi}\sin(\theta_{ps})\cos(\theta_{ps}) - \beta U_p]\Theta(g), (9)$$

$$g = 1 - \phi(b_0 - b_2 S s_p(\theta_{ps})), \qquad (10)$$

where $\Theta(x)$ denotes the unit step function, $k_B T$ is the thermal energy, and $\beta = 1/k_B T$. The factor g expresses the effect of the orientation-dependent excluded volume, where $b_0 = B_0\lambda/a_p = (4 + b_{exc}/2)\lambda$ and $b_2 = -B_2\lambda/a_p = b_{exc}\lambda$. Unoverlapped states exist at $g > 0$. Since $w(\theta_{ps})$ is the weight of each protein orientation, the ensemble average of a quantity χ is given by

$$\langle \chi \rangle = \frac{\int_{-\pi/2}^{\pi/2} \chi w(\theta_{ps}) \, d\theta_{ps}}{\int_{-\pi/2}^{\pi/2} w(\theta_{ps}) \, d\theta_{ps}}. \qquad (11)$$

The quantities Ψ and $\bar{\Psi}$ are the symmetric and asymmetric components of the nematic tensor, respectively, and are determined by eqn (1) and $\langle \sin(\theta_{ps})\cos(\theta_{ps})\rangle = 0$ using eqn (11). When the nematic order is parallel to one of the directions of the membrane principal curvatures ($\theta_{sc} = 0$ or $\pi/2$), $\bar{\Psi} = 0$. The free energy minimum is calculated from $\partial f_p/\partial S = \partial f_p/\partial \theta_{sc} = 0$. More detail is described in Ref. 42.

In this study, we examine the axial force f_{ex} and the equilibrium of the protein binding and unbinding. In experiments, an external force f_{ex} is imposed by optical tweezers and micropipette in order to extend a membrane tube from a liposome. The free energy is give by $F = F_p + U_{mb} - f_{ex}L_{cy}$. This force f_{ex} is balanced with the membrane axial force and is obtained by $\partial F/\partial L_{cy} = 0$ as

$$f_{ex} = 2\pi \frac{\partial f_p}{\partial(1/R_{cy})} + f_{mb}. \qquad (12)$$

The last term f_{mb} represents the force of the bare membrane tube ($\phi = 0$),

$$f_{mb} = \frac{2\pi\kappa_d}{R_{cy}} = \frac{f_0}{R_{cy}C_p}, \qquad (13)$$

where $f_0 = 2\pi\kappa_d C_p$ is the force at $R_{cy}C_p = 1$ and is used as the unit hereafter.

The proteins bind and unbind the membrane with the binding chemical potential μ. The equilibrium of the binding and unbinding is obtained by minimizing $F - \mu N_p$. Hence, the equilibrium protein density is calculated from $\mu = a_p\partial f_p/\partial\phi$. Here, the number N_{lip} of the lipids and the area A remain constant, so that the ensemble is changed from the $N_pN_{lip}AT$ ensemble to $\mu N_{lip}AT$ ensemble.

Unless otherwise specified, we use $d_{el} = 3$ and $a_pC_p^2 = 0.26$,
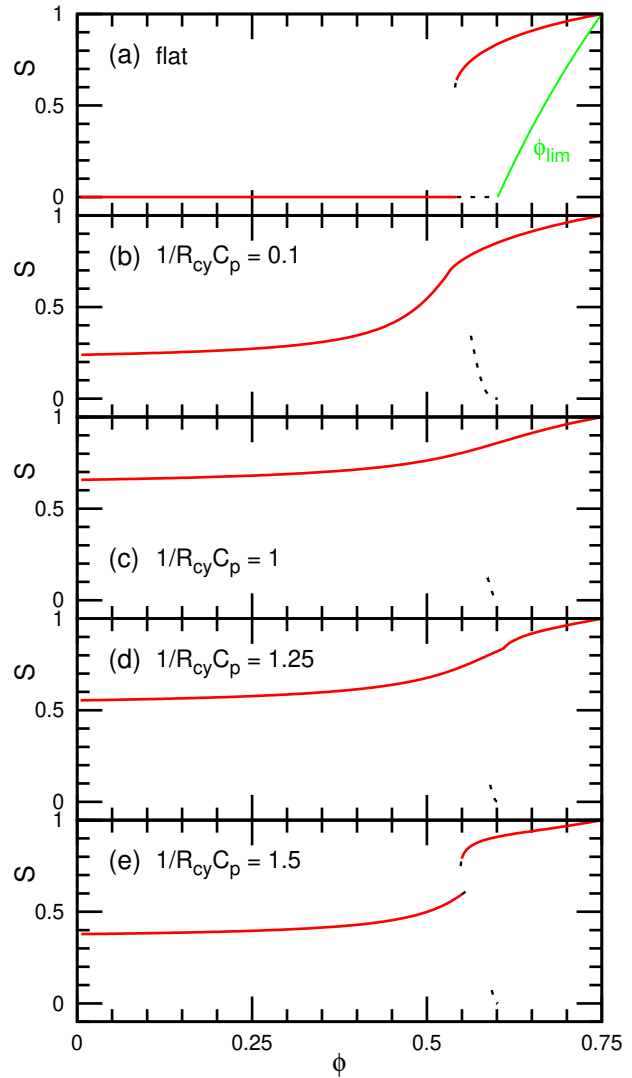

Fig. 2 Orientational degree S of the proteins for $1/R_{cy}C_p = 0$ (flat membrane), 0.1, 1, 1.25, and 1.5 at $\kappa_p/k_B T = 40$ and $d_{el} = 3$. The solid and dashed lines represent the data of stable and metastable states, respectively. The right line in (a) represents the maximum density $\phi_{lim}(S)$ given by eqn (14).

which correspond to the N-BAR domain ($\ell_1 = 7.5$ nm $\ell_2 = 2.5$ nm, and $1/C_p = 15$ nm) [43]. Another area ratio $a_pC_{cy}^2 = 0.26$ is used to examine C_p dependence. The detail of the numerical methods is described in Appendix A.

2.2 Theoretical results

For flat membranes, the proteins exhibit a first-order transition from a randomly oriented state ($S = 0$) to an ordered state ($S > 0$) with increasing protein density ϕ, as shown in Fig. 2(a). This transition density decreases as the elliptic ratio d_{el} increases, and the same behavior is obtained for spherical membranes [42]. For cylindrical membranes, the proteins are oriented on average even at $\phi \to 0$ (see Figs. 2(b)–(e)). The maximum density $\phi_{lim}(S)$ is given by

$$\phi_{lim}(S) = \frac{1}{b_0 - b_2 S/2}, \qquad (14)$$

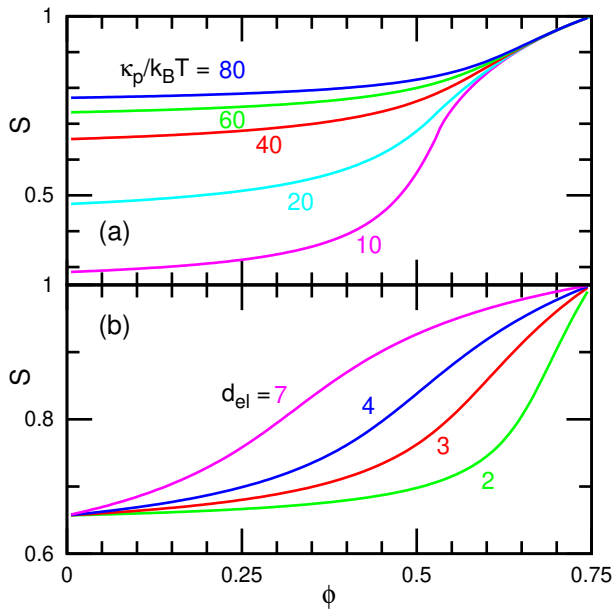Fig. 3 Effects of (a) the bending rigidity κ_p and (b) elliptic ratio d_{el} of the proteins on the density ϕ dependence of the orientational degree S at $1/R_{cy}C_p = 1$. (a) From top to bottom, $\kappa_p/k_BT = 80$, 60, 40, 20, and 10 at $d_{el} = 3$. (b) From top to bottom, $d_{el} = 7$, 4, 3, and 2 at $\kappa_p/k_BT = 40$. The metastable states at $\phi \simeq \phi_{lim}(0)$ are not shown.

Fig. 4 Angles θ_{sc} and θ_{pc} for $1/R_{cy}C_p = 1.25$ and 1.5 at $\kappa_p/k_BT = 40$ and $d_{el} = 3$. Second order and first order transitions occur for $1/R_{cy}C_p = 1.25$ and 1.5, respectively. The solid lines in (a),(b) and dashed lines in (b) represent the data of stable and metastable states, respectively. (d) Two states coexist at $\phi = 0.55$ and $1/R_{cy}C_p = 1.5$. In the inset of (b), the protein states are schematically depicted for low and high protein densities ϕ.

that is independent of the membrane curvature ($\phi_{max} = \phi_{lim}(1)$). The straight line ($S = 0$) for $0 < \phi < \phi_{lim}(0)$ in Fig. 2(a) is divided into two, and the right branch remains even at large tube curvatures, $1/R_{cy}$, although it has a high energy with a narrow width of ϕ (see dashed lines at $\phi \simeq 0.6$ in Figs. 2(b)–(e)). Meanwhile, the left branch connects to the upper branch at $1/R_{cy}C_p \gtrsim 0.1$ (see Fig. 2(b)). Note that it is separated at $1/R_{cy}C_p = 0.01$ (data not shown). At $1/R_{cy}C_p \leq 1$, the proteins prefer to align to the azimuthal direction ($\theta_{pc} = 0$), while the thermal fluctuations disturb it. Hence, the proteins are more ordered (higher S) at higher κ_p (see Fig. 3(a)). At high density ϕ (close to ϕ_{max}), S is dominantly determined by the orientation-dependent excluded volume and the effects increase with increasing d_{el} (see Fig. 3).

At $1/R_{cy}C_p > 1$, the protein preferred direction is tilted either to a positive or negative angle of $\theta_{pc} = \pm \arccos(\sqrt{R_{cy}C_p})$. At low ϕ, the positive and negative angles simultaneously exist, so that the proteins exhibit a symmetric distribution with $\theta_{sc} = 0$ (see Fig. 4). In contrast, at high ϕ, these two angles cannot coexist at the same time owing to the large excluded-volume interactions between them (see the right distributions in Figs. 4(c) and (d)). The transitions between these two states are the second order and first order for $1/R_{cy}C_p \leq 1.3$ and $1/R_{cy}C_p \geq 1.35$ (see Figs. 4(a) and (b)), respectively. The two states coexist at $\phi \simeq 0.55$ and $1/R_{cy}C_p = 1.5$ as shown in Fig. 4(d). Correspondingly, the S–ϕ curves exhibit discrete changes of the slope and position (see Figs. 2(d) and (e)), respectively. In the case of the second-order transition, the excluded-volume interactions push the protein into the azimuthal direction leading to the angular distribution of a single peak near the transition point (see the data at $\phi = 0.6$ in Fig. 4(c)), so that the symmetric peak continuously changes to an asymmetric peak
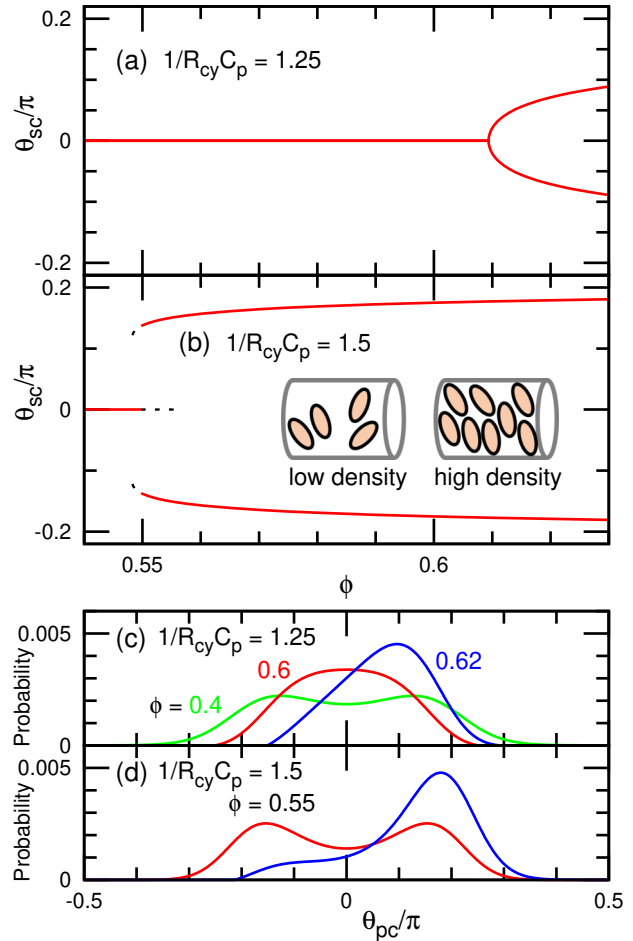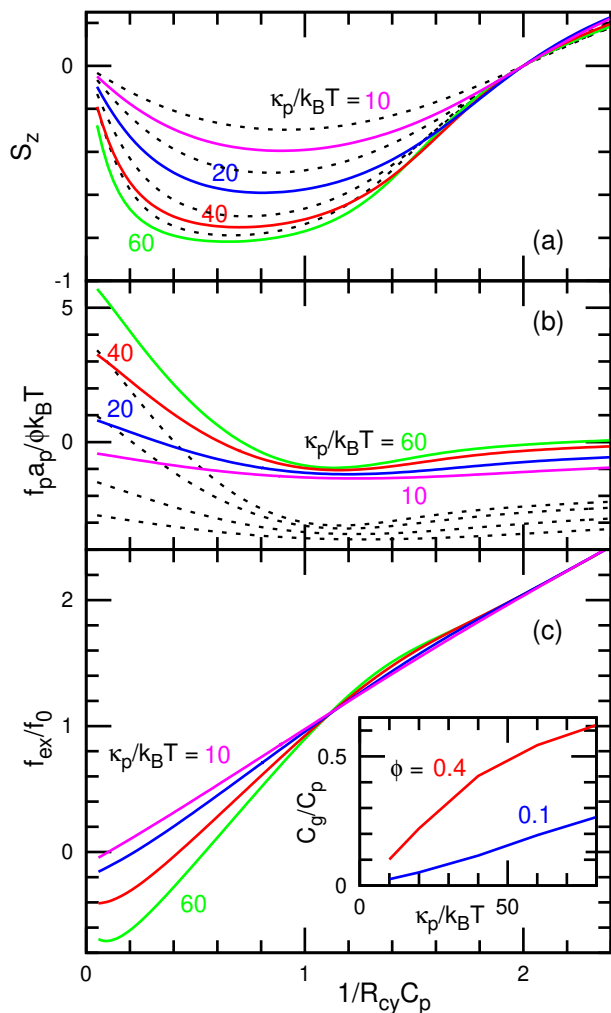
Fig. 5 Dependence on the radius R_{cy} of the membrane tube for a constant protein density at $\kappa_p/k_BT = 40$ and $d_{el} = 3$. (a) Orientational degree S_z along the tube axis. (b) Free energy density f_p of the proteins. (c) Axial force f_{ex} normalized by $f_0 = 2\pi\kappa_d C_p$. The solid and dashed lines represent the data at $\phi = 0.4$ and 0.1, respectively. (a),(c) From top to bottom, $\kappa_p/k_BT = 10$, 20, 40, and 60. (b) From top to bottom, $\kappa_p/k_BT = 60$, 40, 20, and 10. The inset in (c) shows the generation curvature C_g (tube curvature at $f_{ex} = 0$) for $\phi = 0.1$ and 0.4.
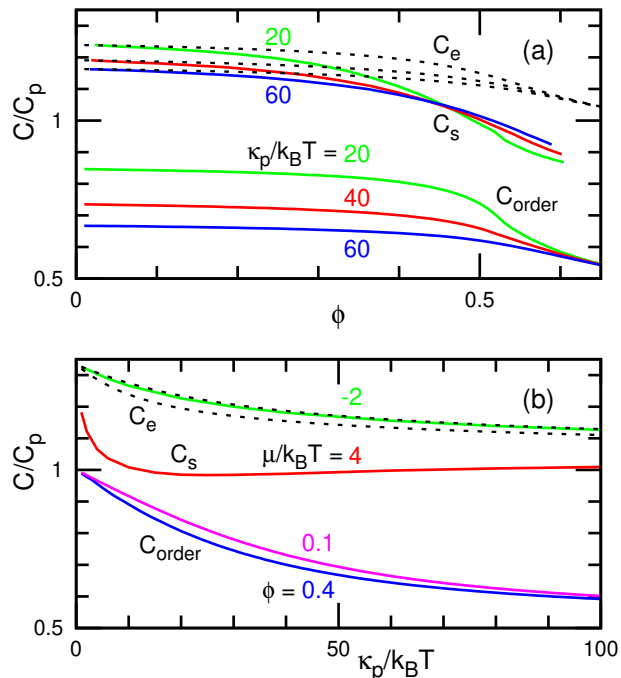

Fig. 6 Order curvature C_{order} (maximum of S), free-energy-minimum curvature C_e, and sensing curvature C_s (maximum binding) of the proteins at $d_{el} = 3$. (a) Dependence on the density ϕ. From top to bottom, $\kappa_p/k_BT = 20$, 40, and 60. (b) Dependence on the protein rigidity κ_p. From top to bottom, $\phi = 0.1$ and 0.4 for C_{order} and C_e, and $\mu/k_BT = -2$ and 4 for C_s. The dashed lines represent C_e.
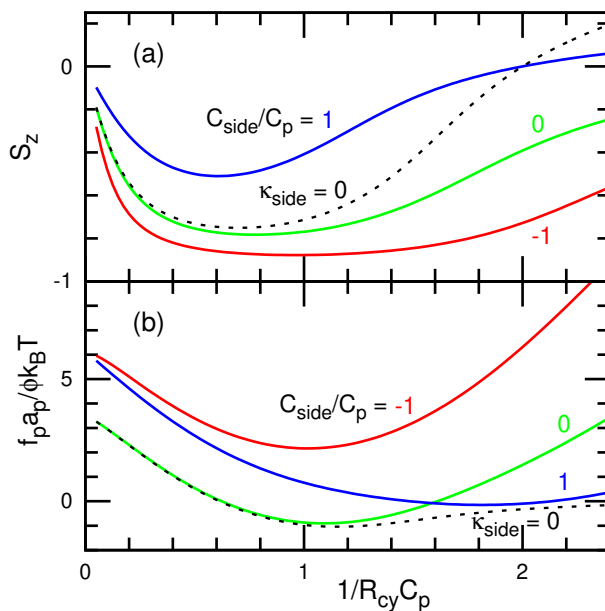

Fig. 7 Effects of the spontaneous curvature C_{side} in the side direction of the proteins on the R_{cy} dependence of (a) the orientational degree S_z along the tube axis and (b) free energy density f_p of the proteins at $\phi = 0.4$, $\kappa_p/k_BT = 40$, and $d_{el} = 3$. The solid lines represent the data for $C_{side}/C_p = -1$, 0, and 1 at $\kappa_{side}/k_BT = 20$. The dashed lines represent the data for no side bending energy ($\kappa_{side} = 0$).
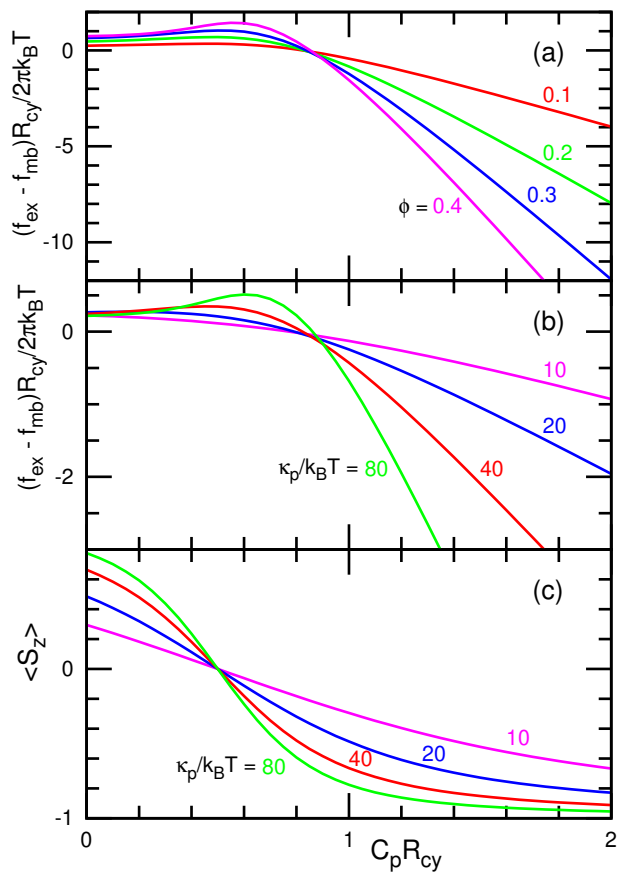
Fig. 8 Dependence on the protein curvature C_p at $a_p C_{cy}^2 = 0.26$ and $d_{el} = 3$. The force f_{ex} for four values of the protein density ϕ and rigidity κ_p are shown in (a) and (b), respectively. (c) Orientational degree S_z for the same data in (b). (a) $\phi = 0.1$, 0.2, 0.3, and 0.4 at $\kappa_p/k_B T = 40$. (b),(c) $\kappa_p/k_B T = 10$, 20, 40, and 80 at $\phi = 0.1$.
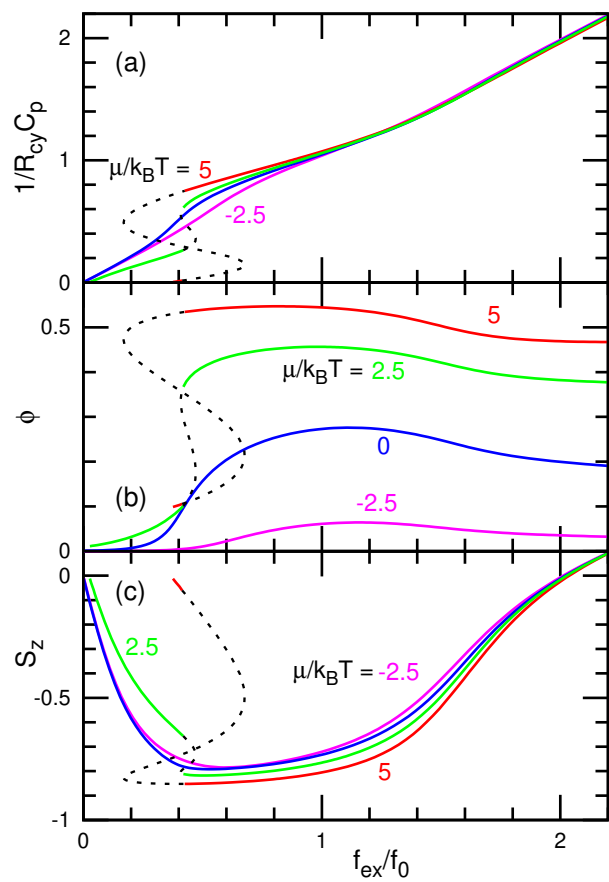
Fig. 9 Force f_{ex} dependence of (a) the curvature $1/R_{cy}$ of the cylindrical membrane, (b) protein density ϕ, and (c) the orientational degree S_z along the tube axis for $\mu/k_B T = -2.5$, 0, 2.5, and 5 at $d_{el} = 3$ and $\kappa_p/k_B T = 60$. The solid lines represent thermal equilibrium states. The dashed lines represent the metastable and free-energy-barrier states. The force is normalized by $f_0 = 2\pi\kappa_d C_p$.

Fig. 10 Force f_{ex} dependence for the proteins with the isotropic bending energy U_{iso} with $\mu/k_B T = -4$, -2, 0, 2, and 4 at $d_{el} = 3$ and $\kappa_{iso}/k_B T = 60$. (a) Curvature $1/R_{cy}$ of the membrane tube. (b) Protein density ϕ. The solid lines represent thermal equilibrium states. The dashed lines represent the metastable and free-energy-barrier states. The force is normalized by $f_0 = 2\pi\kappa_d C_{iso}$.
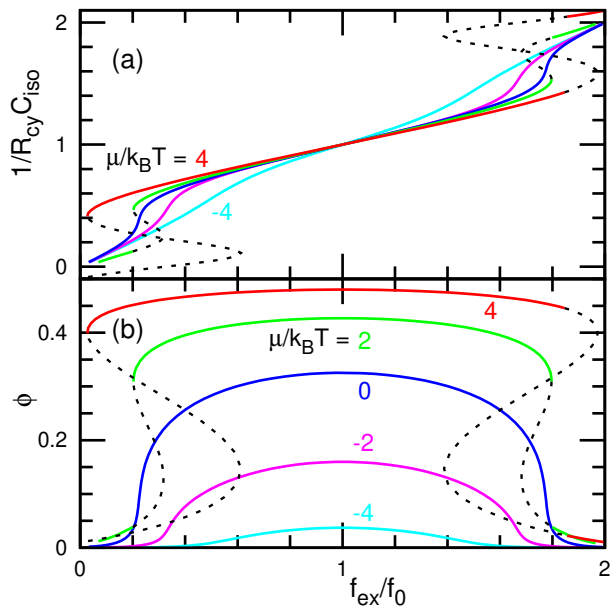
at the transition.

Figure 5 shows the tube curvature $1/R_{cy}$ dependence of the orientational degree S_z along the tube axis, protein free-energy, and axial force f_{ex}. The preferred orientation changes from $\theta_{sc} = 0$ to $\pi/2$ at $1/R_{cy}C_p = 2$, so that S_z changes from negative values ($S_z = -S$) to positive values ($S_z = S$). Interestingly, the orientational order ($S = |S_z|$) has a maximum at $1/2 < 1/R_{cy}C_p < 1$, i.e., less than the matching curvature $1/R_{cy}C_p = 1$ (see Figs. 5(a) and 2). Oppositely, the curvature C_e of the free-energy minimum is higher than the matching curvature (see Fig. 5(b)). These are determined by the competition between the orientational entropy and bending energy. The curvature (C_{order}) of the maximum order and C_e decrease with increasing ϕ and κ_p (see Fig. 6); at $\kappa_p \to \infty$, $C_{order} \to 1/2R_{cy}$, in which the strength of the approximately harmonic potential of U_p for $\theta_{pc} \ll 1$ (i.e., $\partial^2 U_p/\partial \theta_{pc}^2|_{\theta_{pc}=0}$) is maximum. The amplitudes of the order and the depth of free-energy minimum increase with increasing κ_p (see Figs. 5(a) and (b), respectively). Corresponding to the larger energy change in f_p, the axial force f_{ex} deviates more from the value of the bare membrane (f_{mb} given by eqn (13)) at higher κ_p (see Fig. 5(c)). Spontaneously formed membrane tubes require no axial force (i.e., $f_{ex} = 0$). The generation curvature C_g of this spontaneous tube increases with increasing κ_p and ϕ (see the inset of Fig. 5(c)), i.e., a narrower tube is generated. Note that C_g also depends on the bending rigidity κ_d of the bare membrane in contrast to C_{order} and C_e.

Next, we examine the effects of the protein bending energy in the side direction (see Fig. 7). At zero side spontaneous curvature ($C_{side} = 0$), the proteins more align in the azimuthal direction

with increasing κ_{side}, since the curvature $C_{\ell 2}$ in the side direction becomes closer to C_{side}. This effect is pronounced at narrow tubes, whereas it is negligible for $1/R_{cy}C_p < 1$. For a negative value of C_{side}, C_{order} and C_e become close to C_p, and the proteins more align in a wider range of $1/R_{cy}$. For a positive value of C_{side}, C_{order} and C_e become deviated from C_p, and the proteins less align. The generation curvature slightly increases with increasing C_{side}: $C_g = 0.412$, 0.421, and 0.448 at $C_{side} = -1$, 0, and 1, respectively, for the condition used in Fig. 7.

We have fixed the protein curvature C_p until here. Figure 8 shows the effects of C_p variation with maintaining the other parameters. As C_p changes from null to $1/R_{cy}$, the nematic orientation changes from the axial direction ($\theta_{sc} = \pi/2$) to the azimuthal direction ($\theta_{sc} = 0$) (see the left half of Fig. 8(c)). This change becomes steeper at higher κ_p. During this change, the axial force f_{ex} is almost constant, although a small peak appears for high κ_p and/or high ϕ (see the left regions of Figs. 8(a) and (b)). This is due to little change in the bending energy, because the proteins can find their preferred curvature by adjusting their orientation. For $C_p \gtrsim 1/R_{cy}$, f_{ex} almost linearly decreases, and the slope increases with increasing κ_p and ϕ (see the right region of Figs. 8(a) and (b)). These dependencies qualitatively agree with the results of our previous meshless membrane simulations [41,57,59]. A quantitative comparison is described in Sec. 3.2.

Finally, we examine the equilibrium of the protein binding and unbinding. As the binding chemical potential μ increases, more proteins bind onto the membrane. The protein binding exhibits a first-order transition from a wide tube with low ϕ to a narrow tube with high ϕ at small force, $f_{ex} < f_0$ (see Fig. 9). This transition agrees with the observation of the coexistence of two tubes with different R_{cy} and ϕ in the experiments of an I-BAR protein [17]. The force-dependence curves shown in Fig. 9 are asymmetric and exhibit weak dependence at $f_{ex} > f_0$, owing to the adjustment of the protein orientation that reduces a change in the protein bending energy (see Fig. 9(c)). These behaviors are different from the binding of proteins with an isotropic spontaneous curvature [30], where the f_{ex}–$1/R_{cy}$ and f_{ex}–ϕ curves are point symmetric and reflection symmetric to $f_{ex} = f_0$, respectively.

The protein binding has a maximum in the variation of the tube curvature (compare Figs. 9(a) and (b)). This curvature is called sensing curvature (denoted C_s) and can be calculated from $\partial \phi/\partial (1/R_{cy}) = 0$. Interestingly, C_s is varied by μ and κ_p (see Fig. 6). For low ϕ at low μ, C_s approach C_e, since the excluded volume gives negligible effects. For high μ ($\phi \gtrsim 0.5$ in Fig. 6(a)), C_s becomes lower than C_p, and ϕ has a broad peak. A similar C_s dependence on the tube curvature has been reported in the experiments of the BAR proteins [17,18]. It indicates the anisotropic interaction of the BAR proteins.

The asymmetry of the force-dependence curves is caused not by the orientation-dependent excluded volume but by the anisotropy of the protein bending energy. To clearly show it, the force-dependence curves for the elliptic proteins with an isotropic spontaneous curvature C_{iso} are plotted in Fig. 10. The proteins have a bending energy

$$U_{iso} = \frac{\kappa_{iso} a_p}{2}(C_1 + C_2 - C_{iso})^2, \qquad (15)$$

instead of U_p. Note that the anisotropic bending energy U_p with $\kappa_p = \kappa_{side}$ and $C_p = C_{side}$ does not coincide to U_{iso} except for the case of $\theta_{pc} = 0$ or $\pi/2$. The f_{ex}–$1/R_{cy}$ and f_{ex}–ϕ curves become point symmetric and reflection symmetric to $f_{ex} = f_0$, respectively, and the first-order transitions occur both at small and large forces symmetrically. The transition points are almost constant for a variation in μ. This is due to the excluded-volume dependence on the protein orientation, since the transition points move outwards in the case of orientation-independent excluded volume[30].

3 Simulation

3.1 Simulation model

A fluid membrane is represented by a self-assembled single-layer sheet of N particles. The position and orientational vectors of the i-th particle are $\boldsymbol{r}_i$ and $\boldsymbol{u}_i$, respectively. The membrane particles interact with each other via a potential $U = U_{rep} + U_{att} + U_{bend} + U_{tilt}$. The potential U_{rep} is an excluded volume interaction with diameter σ for all pairs of particles. The solvent is implicitly accounted for by an effective attractive potential U_{att}. The details of the meshless membrane model and protein rods are described in Ref. 66 and Refs. 57,59, respectively. We employ the parameter sets used in Ref. 59.

The bending and tilt potentials are given by $U_{bend}/k_B T = (k_{bend}/2)\sum_{i<j}(\boldsymbol{u}_i - \boldsymbol{u}_j - C_{bd}\hat{\boldsymbol{r}}_{i,j})^2 w_{cv}(r_{i,j})$ and $U_{tilt}/k_B T = (k_{tilt}/2)\sum_{i<j}[(\boldsymbol{u}_i \cdot \hat{\boldsymbol{r}}_{i,j})^2 + (\boldsymbol{u}_j \cdot \hat{\boldsymbol{r}}_{i,j})^2]w_{cv}(r_{i,j})$, respectively, where $\boldsymbol{r}_{i,j} = \boldsymbol{r}_i - \boldsymbol{r}_j$, $r_{i,j} = |\boldsymbol{r}_{i,j}|$, $\hat{\boldsymbol{r}}_{i,j} = \boldsymbol{r}_{i,j}/r_{i,j}$, $w_{cv}(r_{i,j})$ is a weight function. The spontaneous curvature C_0 of the membrane is given by $C_0\sigma = C_{bd}/2$.[66] In this study, $C_0 = 0$ and $k_{bend} = k_{tilt} = 10$ are used except for the membrane particles belonging to the protein rods.

An anisotropic protein and membrane underneath it are together modeled as a rod that is a linear chain of N_{sg} membrane particles[57]. We use $N_{sg} = 5$ and 10 with the density $\phi = N_{sg}N_{rod}/N = 0.167$. The protein rods have spontaneous curvatures C_{rod} along the rod axis and have no spontaneous (side) curvatures perpendicular to the rod axis. The protein-bound membrane are more rigid than the bare membrane: the values of k_{bend} and k_{tilt} are k_r times higher than those of the bare membrane.

The membrane has mechanical properties that are typical of lipid membranes: the bare membrane has a bending rigidity $\kappa/k_B T = 16.1 \pm 0.02$, area of the tensionless membrane per particle $a_0/\sigma^2 = 1.2778 \pm 0.0002$, area compression modulus $K_A\sigma^2/k_B T = 83.1 \pm 0.4$, edge line tension $\Gamma\sigma/k_B T = 5.73 \pm 0.04$[57], and the Gaussian modulus $\bar{\kappa}/\kappa = -0.9 \pm 0.1$[67]. The bending rigidity is calculated by eqn (13), which is slightly greater than the value (15 ± 1) estimated by thermal undulation[66]. The membrane tube with a length of L_{cy} is connected by the periodic boundary, and the tube volume can be freely varied. Molecular dynamics with a Langevin thermostat is employed[66,68]. The dependence on the rod curvature C_{rod} was calculated at $L_{cy} = 48\sigma$ and $N = 2400$ in Ref. 59 using the replica-exchange method[69,70]. The dependence on the tube radius was calculated at $k_r = 4$ and $N = 4800$ in this study.
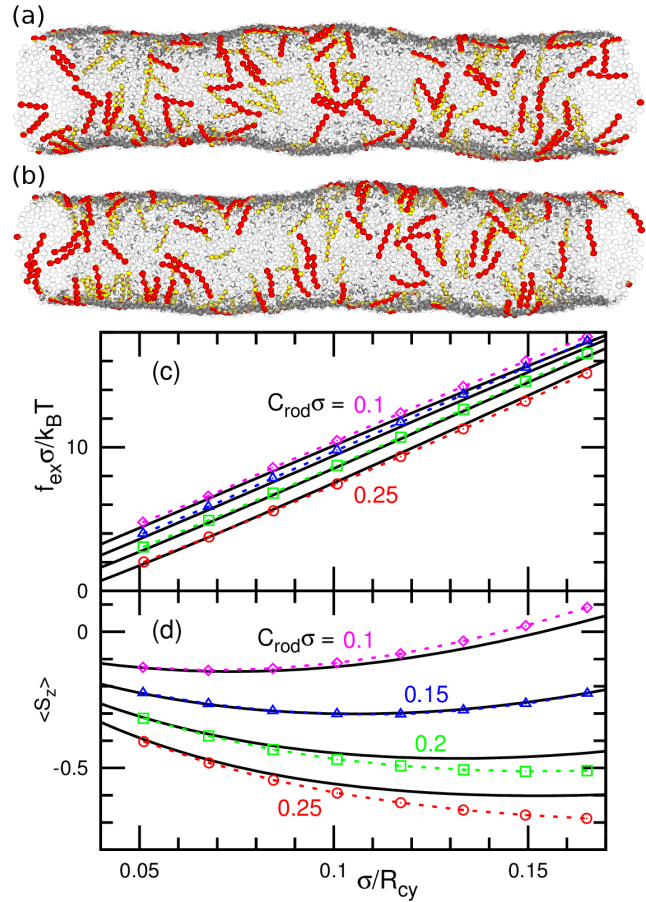

Fig. 11 Membrane simulations of the short protein rods of $N_{sg} = 5$ at $k_r = 4$. (a),(b) Snapshots for (a) $C_{rod}\sigma = 0.1$ and (b) $C_{rod}\sigma = 0.25$ at $L_{cy}/\sigma = 96$ ($R_{cy}/\sigma = 9.92$ and 9.91, respectively). A protein rod is displayed as a chain of spheres whose halves are colored in red and in yellow. The orientational vector $\boldsymbol{u}_i$ lies along the direction from the yellow to red hemispheres. Transparent gray particles represent membrane particles. (c),(d) Dependence of (c) the axial force f_{ex} and (d) orientational order $\langle S_z \rangle$ along the membrane tube on the tube radius R_{cy} for $C_{rod}\sigma = 0.1$, 0.15, 0.2, and 0.25. The symbols with dashed lines represent the simulation data. The black solid lines represent the theoretical results.
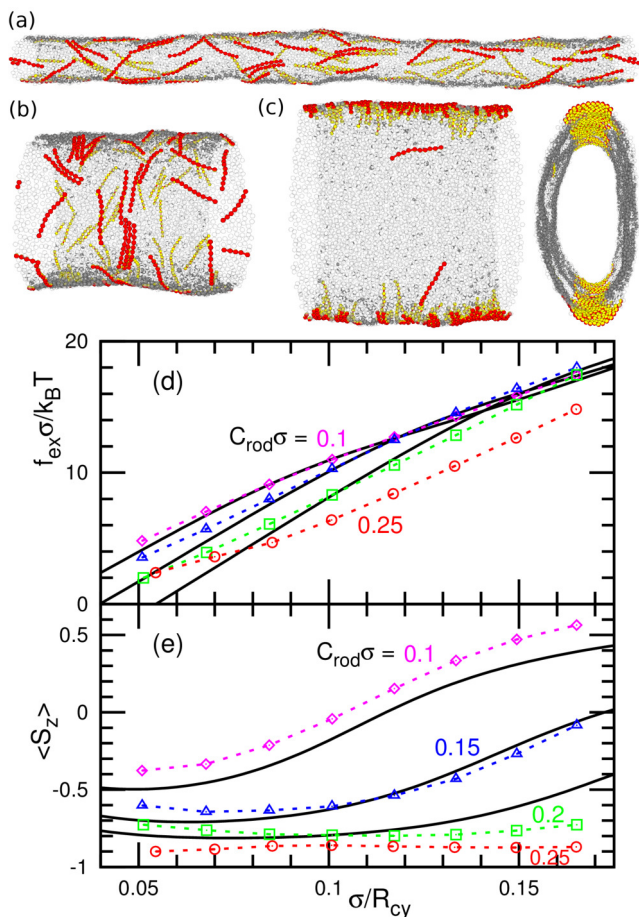
Fig. 12 Membrane simulations of the long protein rods of $N_{sg} = 10$ at $k_r = 4$. (a)–(c) Snapshots for (a),(b) $C_{rod}\sigma = 0.1$ and (c) $C_{rod}\sigma = 0.25$. (a) $L_{cy}/\sigma = 160$ ($R_{cy}/\sigma = 6.05$). (b),(c) $L_{cy}/\sigma = 48$ ($R_{cy}/\sigma = 19.66$ and 18.37, respectively). The front and side views are displayed in (c). (d),(e) Dependence of (d) the axial force f_{ex} and (e) orientational order $\langle S_z \rangle$ along the membrane tube on the tube radius R_{cy} for $C_{rod}\sigma = 0.1$, 0.15, 0.2, and 0.25. The symbols with dashed lines represent the simulation data. The black solid lines represent the theoretical results for $C_{rod}\sigma = 0.1$, 0.15, and 0.2.
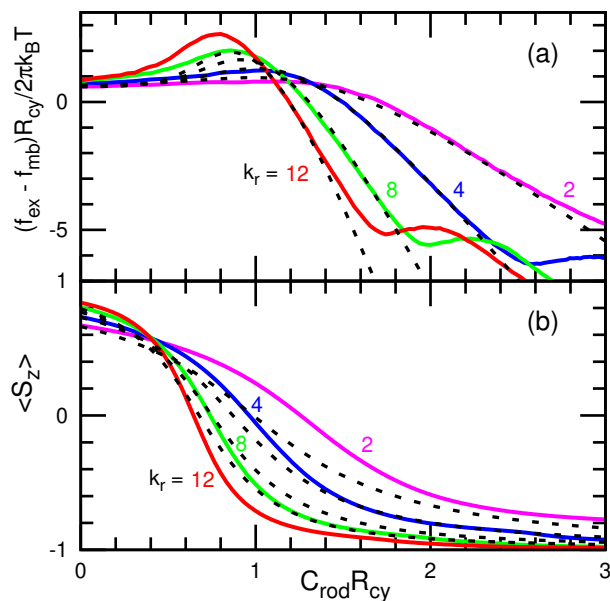

Fig. 13 (a),(b) Dependence of (a) the axial force f_{ex} and (b) orientational order $\langle S_z \rangle$ along the membrane tube on the rod curvature C_{rod} for the bending rigidity ratio $k_r = 2$, 4, 8, and 12 at $N_{sg} = 10$ and $R_{cy}/\sigma = 9.89$. The solid lines represent the simulation data. The black dashed lines represent the theoretical results. The force generated by the proteins is normalized as $(f_{ex} - f_{mb})R_{cy}/2\pi k_B T$, where f_{mb} is the force of the bare membrane. The simulation data (solid lines) are reproduced from Ref. 59.

3.2 Comparison of simulation and theoretical results

Figure 11 and Figs. 12,13 show the simulation and theoretical results for the short and long protein rods ($N_{sg} = 5$ and 10), respectively. Since the simulated proteins do not have an elliptic shape and are flexible, the protein parameters are adjusted as follows. For the short rods, we used the orientational degree S_z at $C_{rod}\sigma = 0.15$ (the second line from the top in Fig. 11(d)) for a fit and obtained $\kappa_p = 30 k_B T$ and $C_{rod}/C_p = 2$ for $a_p = N_{sg}a_0$ and $d_{el} = 3$. This parameter set reproduces the simulation data of S_z and f_{ex} at different values of C_{rod} very well. Thus, this theory can quantitatively describe the behavior of the short proteins.

However, less agreement is obtained for the long rods of $N_{sg} = 10$ (see Figs. 12 and 13). It is due to the protein assembly induced by the membrane-mediated attractive interactions between the proteins (see the snapshots in Figs. 12(a)–(c)). At a high rod curvature ($C_{rod}\sigma = 0.25$), the proteins assemble in the azimuthal direction, and the membrane deforms into an elliptic tube, as shown in Fig. 12(c). For longer (narrower) and shorter (wider) tubes, cylindrical and triangular shapes are formed (see Movie 1 in ESI). Thus, large negative values of S_z (Fig. 12(e)) and non-monotonic dependence of f_{ex} for $C_{rod}R_{cy} \gtrsim 2.5$ ($C_{rod}\sigma \gtrsim 0.25$) at $k_r = 4$ (Fig. 13(a)) are obtained. In the elliptic and triangular membranes, the proteins align in the azimuthal direction, so that their stabilities can be analyzed by assuming a fixed protein orientation as reported in Ref. 41. More detail of this assembly is described in Refs. 41,57,59.

For a lower rod curvature ($C_{rod}\sigma \leq 0.2$) of the long rods at $k_r = 4$, the azimuthal assembly does not occur, but clusters of a

few proteins appear as shown in Figs. 12(a) and (b). We fitted the linear-decrease region of the force-dependence curve in Fig. 13(a) at $C_{rod}R_{cy} > 1$ and obtained $\kappa_p/k_BT = 60, 90, 120,$ and 150 with $C_{rod}/C_p = 2.5, 2.05, 1.7,$ and 1.5 for $k_r = 2, 4, 8,$ and 12, respectively, at $a_p = N_{sg}a_0$ and $d_{el} = 7$. The orientational orders S_z calculated by these parameter sets show quantitative deviation from the simulation data, although they capture qualitative behavior (see Figs. 12(e) and 13(b)). Moreover, the other regions of the force-dependence curves have quantitative differences: the heights of peaks at $C_{rod}R_{cy} < 1$ in Fig. 13(a) deviate from the simulation values, and the slopes at $\sigma/R_{cy} < 0.1$ in Fig. 12(d) are different. Although the present theory assumes the uniform lateral distribution of the proteins, the protein clusters can bend the membrane more strongly as demonstrated by the formation of the elliptic tube. Therefore, we consider that the clusters effectively work as large or rigid proteins. The greater values of κ_p and C_p obtained by the fits support this mechanism. Thus, for a quantitative prediction of a long protein (i.e., a large elliptic ratio d_{el}), it is significant to include the effects of the protein clusters.

4 Summary and discussions

We have studied the equilibrium states of the anisotropic curvature-inducing proteins theoretically and compared them with the simulation results. The protein is assumed to have an elliptic shape with a bending rigidity and spontaneous curvature mainly along the major axis of the protein. On narrow membrane tubes, the proteins exhibit a first-order nematic transition with increasing protein density as reported in our previous paper[42]. Here, we found that this transition becomes the second order on the tubes with intermediate radii. In our previous study, the proteins on a membrane with a fixed shape have been considered. In this study, we extended the theory to proteins on membrane tubes which radius is not fixed and in the binding/unbinding equilibrium. We found that the protein binding affects the membrane axial force differently for wide and narrow tubes. For wide tubes, the force is reduced by the binding. In contrast, it is only slightly modified for narrow tubes, on which the proteins are tilted from the azimuthal direction. With increasing binding chemical potential, a first-order transition between two tube radii with different protein densities occurs only once at the wide tubes, whereas the proteins with an isotropic bending energy exhibit the transition twice. For the short proteins, this theory reproduces the protein orientation and axial force obtained by the meshless simulations very well. In contrast, the long proteins have large membrane-mediated attractive interactions so that resultant protein clusters modify the mean orientation and axial force. However, the theory still holds qualitative dependency.

Moreover, we found that the tube curvatures for the maximum protein binding (sensing) and orientational order are different from the protein spontaneous curvature C_p. The sensing curvature is higher than C_p at low protein density and coincides to the curvature of the free energy minimum. This is contrast to isotropic proteins[30] which sensing curvature is constant. The order curvature is lower than C_p and decreases with increasing protein density and bending rigidity. These dependencies are caused by the variation in the protein orientation. Previously, the proteins are often assumed to orient to the azimuthal direction. Even at the tube curvature close to C_p, the orientational fluctuations modify the average protein behavior. Thus, it is important to take the orientational degree of freedom into account.

Since the theory for the isotropic bending energy has been well established, it has been employed even in the analysis for the experiments of the BAR proteins[17,18,32]. In this study, however, we have clarified that the anisotropy of the bending energy largely changes the membrane–protein interactions such as the sensing curvature. Therefore, the effects of the protein orientation should be included for more quantitative analysis.

We also showed that the protein side curvature (spontaneous curvature along the protein minor axis) modifies the protein binding. The proteins are oriented less or more strongly in the azimuthal direction for a positive or negative side curvature, respectively. It has been reported that the side curvature of the opposite sign to C_p can induce the formation of an egg-carton shape[37,38] and network structures[58]. However, in many previous studies, the side curvature has not been considered. When the proteins or objects strongly bind the membrane as in coarse-grained molecular simulations[50,52], the proteins effectively have a large negative side curvature. Such a large side curvature can change the orientation direction perpendicularly leading to the tip-to-tip protein assembly as discussed in Ref. 40.

In the present theory, we consider only an excluded-volume interaction between proteins. Bound proteins can attract each other via direct and/or membrane-mediated interactions. In particular, BAR proteins typically form helical alignments in dense-packed conditions. Such a chiral interaction can largely modify the protein assembly and membrane shape[56,61]. To reproduce them, additional interactions are required to account for. However, for a sufficiently low protein density, such additional interactions are negligibly weak. Hence, the present theory can be used to estimate the bending rigidity and curvature of bound proteins in experiments and atomistic simulations. These mechanical parameters are keys to quantitatively understand the curvature sensing and generation of proteins.

Author contributions

H.N. conceived the research. H.N. wrote the calculation code for the theoretical analysis with help of C.T. C.T. calculated the factors of excluded volume interactions. H.N. conducted the theoretical calculations and simulations, analyzed the data, and wrote the manuscript. All authors reviewed the manuscript and approved it.

Conflicts of interest

There are no conflicts to declare.

Acknowledgements

A Calculation method for the present theory

The quantities Ψ and $\bar{\Psi}$ are single-valued functions of S, so that they can be calculated by root-finding algorithms such as the bisection method. Alternatively, for $\phi \leq 1/(b_0 + b_2/2)$, where $g > 0$ for any value of S, S can be calculated by solving the quadratic equation of $S = (q_0 + q_1 S)/(p_0 + p_1 S)$ for given Ψ and $\bar{\Psi}$ as

$$S = \frac{q_1 - p_0 + \sqrt{(q_1 - p_0)^2 + 4q_0 p_1}}{2p_1}, \tag{16}$$

where

$$p_0 = \int_{-\pi/2}^{\pi/2} w_0 \, d\theta_{\mathrm{ps}}, \qquad p_1 = \int_{-\pi/2}^{\pi/2} w_1 \, d\theta_{\mathrm{ps}},$$

$$q_0 = \int_{-\pi/2}^{\pi/2} 2s_{\mathrm{p}}(\theta_{\mathrm{ps}}) w_0 \, d\theta_{\mathrm{ps}}, \quad q_1 = \int_{-\pi/2}^{\pi/2} 2s_{\mathrm{p}}(\theta_{\mathrm{ps}}) w_1 \, d\theta_{\mathrm{ps}},$$

$$w_0 = (1 - b_0 \phi) \exp[\Psi s_{\mathrm{p}}(\theta_{\mathrm{ps}}) + \bar{\Psi} \sin(\theta_{\mathrm{ps}}) \cos(\theta_{\mathrm{ps}}) - \beta U_{\mathrm{p}}],$$

$$w_1 = b_2 \phi s_{\mathrm{p}}(\theta_{\mathrm{ps}}) \exp[\Psi s_{\mathrm{p}}(\theta_{\mathrm{ps}}) + \bar{\Psi} \sin(\theta_{\mathrm{ps}}) \cos(\theta_{\mathrm{ps}}) - \beta U_{\mathrm{p}}].$$

At $\phi \simeq 1/b_0$, S can be a multivalued function of Ψ. For $1/(b_0 + b_2/2) < \phi < \phi_{\max}$, large values of S can be calculated by the iteration of eqn (1) by updating S. However, the smaller values of S should be calculated by the former method ($\Psi(S)$). In this study, $\partial f_{\mathrm{p}}/\partial(1/R_{\mathrm{cy}})$ and $\partial f_{\mathrm{p}}/\partial \phi$ are calculated by the central difference method.

Notes and references

1 H. T. McMahon and J. L. Gallop, *Nature*, 2005, **438**, 590–596.

2 S. Suetsugu, S. Kurisu and T. Takenawa, *Physiol. Rev.*, 2014, **94**, 1219–1248.

3 L. Johannes, R. G. Parton, P. Bassereau and S. Mayor, *Nat. Rev. Mol. Cell. Biol.*, 2015, **16**, 311–321.

4 F. Brandizzi and C. Barlowe, *Nat. Rev. Mol. Cell Biol.*, 2013, **14**, 382–392.

5 J. H. Hurley, E. Boura, L.-A. Carlson and B. Różycki, *Cell*, 2010, **143**, 875–887.

6 H. T. McMahon and E. Boucrot, *Nat. Rev. Mol. Cell. Biol.*, 2011, **12**, 517–533.

7 T. Baumgart, B. R. Capraro, C. Zhu and S. L. Das, *Annu. Rev. Phys. Chem.*, 2011, **62**, 483–506.

8 C. Has and S. L. Das, *Biochim. Biophys. Acta*, 2021, **1865**, 129971.

9 T. Itoh and P. De Camilli, *Biochim. Biophys. Acta*, 2006, **1761**, 897–912.

10 M. Masuda and N. Mochizuki, *Semin. Cell Dev. Biol.*, 2010, **21**, 391–398.

11 C. Mim and V. M. Unger, *Trends Biochem. Sci.*, 2012, **37**, 526–533.

12 A. Frost, R. Perera, A. Roux, K. Spasov, O. Destaing, E. H. Egelman, P. De Camilli and V. M. Unger, *Cell*, 2008, **132**, 807–817.

13 B. Sorre, A. Callan-Jones, J. Manzi, B. Goud, J. Prost, P. Bassereau and A. Roux, *Proc. Natl. Acad. Sci. USA*, 2012, **109**, 173–178.

14 C. Zhu, S. L. Das and T. Baumgart, *Biophys. J.*, 2012, **102**, 1837–1845.

15 Y. Tanaka-Takiguchi, T. Itoh, K. Tsujita, S. Yamada, M. Yanagisawa, K. Fujiwara, A. Yamamoto, M. Ichikawa and K. Takiguchi, *Langmuir*, 2013, **29**, 328–336.

16 J. Adam, N. Basnet and N. Mizuno, *Sci. Rep.*, 2015, **5**, 15452.

17 C. Prévost, H. Zhao, J. Manzi, E. Lemichez, P. Lappalainen, A. Callan-Jones and P. Bassereau, *Nat. Commun.*, 2015, **6**, 8529.

18 F.-C. Tsai, M. Simunovic, B. Sorre, A. Bertin, J. Manzi, A. Callan-Jones and P. Bassereau, *Soft Matter*, 2021, **17**, 4254–4265.

19 A. Roux, G. Koster, M. Lenz, B. Sorre, J.-B. Manneville, P. Nassoy and P. Bassereau, *Proc. Natl. Acad. Sci. USA*, 2010, **107**, 4141–4146.

20 K. R. Rosholm, N. Leijnse, A. Mantsiou, V. Tkach, S. L. Pedersen, V. F. Wirth, L. B. Oddershede, K. J. Jensen, K. L. Martinez, N. S. Hatzakis, P. M. Bendix, A. Callan-Jones and D. Stamou, *Nat. Chem. Biol.*, 2017, **13**, 724–729.

21 P. B. Canham, *J. Theor. Biol.*, 1970, **26**, 61–81.

22 W. Helfrich, *Z. Naturforsch*, 1973, **28c**, 693–703.

23 R. Lipowsky, *J. Phys. II France*, 1992, **2**, 1825–1840.

24 P. Sens, *Phys. Rev. Lett.*, 2004, **93**, 108103.

25 L. Foret, *Eur. Phys. J. E*, 2014, **37**, 42.

26 F. Frey and U. S. Schwarz, *Soft Matter*, 2020, **16**, 10723–10733.

27 C. Tozzi, N. Walani and M. Arroyo, *New J. Phys.*, 2019, **21**, 093004.

28 H. Noguchi, *Phys. Rev. E*, 2021, **104**, 014410.

29 Q. Goutaland, F. van Wijland, J.-B. Fournier and H. Noguchi, *Soft Matter*, 2021, **17**, 5560–5573.

30 H. Noguchi, *Soft Matter*, 2021, **17**, 10469–10478.

31 N. S. Gov, *Phil. Trans. R. Soc. B*, 2018, **373**, 20170115.

32 Z. Wu, M. Su, C. Tong, M. Wu and J. Liu, *Nat. Commun.*, 2018, **9**, 136.

33 N. Tamemoto and H. Noguchi, *Sci. Rep.*, 2020, **10**, 19582.

34 N. Tamemoto and H. Noguchi, *Soft Matter*, 2021, **17**, 6589–6596.

35 J.-B. Fournier, *Phys. Rev. Lett.*, 1996, **76**, 4436–4439.

36 D. Kabaso, E. Gongadze, P. Elter, U. van Rienen, J. Gimsa, V. Kralj-Iglič and A. Iglič, *Mini Rev. Med. Chem.*, 2011, **11**, 272–282.

37 P. G. Dommersnes and J.-B. Fournier, *Eur. Phys. J. B*, 1999, **12**, 9–12.

38 P. G. Dommersnes and J.-B. Fournier, *Biophys. J.*, 2002, **83**, 2898–2905.

39 Y. Schweitzer and M. M. Kozlov, *PLoS Comput. Biol.*, 2015, **11**, e1004054.

40 H. Noguchi and J.-B. Fournier, *Soft Matter*, 2017, **13**, 4099–4111.

41 H. Noguchi, *J. Chem. Phys.*, 2015, **143**, 243109.

42 C. Tozzi, N. Walani, A.-L. L. Roux, P. Roca-Cusachs and M. Arroyo, *Soft Matter*, 2021, **17**, 3367–3379.

43 A.-L. L. Roux, C. Tozzi, N. Walani, X. Quiroga, D. Zalvidea, X. Trepat, M. Staykova, M. Arroyo and P. Roca-Cusachs, *Nat. Commun.*, 2021, **12**, 6550.

44 E. S. Nascimento, P. Palffy-Muhoray, J. M. Taylor, E. G. Virga and X. Zheng, *Phys. Rev. E*, 2017, **96**, 022704.

45 M. Müller, K. Katsov and M. Schick, *Phys. Rep.*, 2006, **434**, 113–176.

46 M. Venturoli, M. M. Sperotto, M. Kranenburg and B. Smit, *Phys. Rep.*, 2006, **437**, 1–54.

47 H. Noguchi, *J. Phys. Soc. Jpn.*, 2009, **78**, 041007.

48 A. Arkhipov, Y. Yin and K. Schulten, *Biophys. J.*, 2008, **95**, 2806–2821.

49 H. Yu and K. Schulten, *PLoS Comput. Biol.*, 2013, **9**, e1002892.

50 M. Simunovic, A. Srivastava and G. A. Voth, *Proc. Natl. Acad. Sci. USA*, 2013, **110**, 20396–20401.

51 J. Gómez-Llobregat, F. Elías-Wolff and M. Lindén, *Biophys. J.*, 2016, **110**, 197–204.

52 A. D. Olinger, E. J. Spangler, P. B. S. Kumar and M. Laradji, *Faraday Discuss.*, 2016, **186**, 265–275.

53 K. Takemura, K. Hanawa-Suetsugu, S. Suetsugu and A. Kitao, *Sci. Rep.*, 2017, **7**, 6808.

54 M. I. Mahmood, H. Noguchi and K. Okazaki, *Sci. Rep.*, 2019, **9**, 14557.

55 N. Ramakrishnan, P. B. Sunil Kumar and J. H. Ipsen, *Biophys. J.*, 2013, **104**, 1018–1028.

56 A. Behera, G. Kumar, S. A. Akram and A. Sain, *Soft Matter*, 2021, **17**, 7953–7962.

57 H. Noguchi, *EPL*, 2014, **108**, 48001.

58 H. Noguchi, *Sci. Rep.*, 2016, **6**, 20935.

59 H. Noguchi, *Phys. Rev. E*, 2016, **93**, 052404.

60 H. Noguchi, *Soft Matter*, 2017, **13**, 7771–7779.

61 H. Noguchi, *Sci. Rep.*, 2019, **9**, 11721.

62 A.-S. Smith, E. Sackmann and U. Seifert, *Phys. Rev. Lett.*, 2004, **92**, 208101.

63 M. Tanemura and T. Matsumoto, *Zeit. Krist.*, 1997, **212**, 637–647.

64 U. Seifert, *Adv. Phys.*, 1997, **46**, 13–137.

65 S. Svetina, *ChemPhysChem*, 2009, **10**, 2769–2776.

66 H. Shiba and H. Noguchi, *Phys. Rev. E*, 2011, **84**, 031926.

67 H. Noguchi, *J. Chem. Phys.*, 2019, **151**, 094903.

68 H. Noguchi, *J. Chem. Phys.*, 2011, **134**, 055101.

69 K. Hukushima and K. Nemoto, *J. Phys. Soc. Jpn.*, 1996, **65**, 1604–1608.

70 Y. Okamoto, *J. Mol. Graph. Model.*, 2004, **22**, 425–439.